

Pseudocapacitive lithium-rich disordered rocksalt vanadium oxide with 3D lithium-ion transport pathways for high-performance lithium-ion capacitor

Han Zhao

Shandong University

Minghao Hua

Shandong University

Chongxing Li

Shandong University

Tong Li

Shandong University

Yuying Qin

Shandong University

Shuxian Zhang

Shandong University

Xiaohang Lin

Shandong University

Longwei Yin

Shandong University <https://orcid.org/0000-0003-3768-6846>

Rutao Wang (✉ rtwang@sdu.edu.cn)

Shandong University

Article

Keywords: Lithium-rich disordered rocksalt vanadium oxide, Pseudocapacitance, Lithium-ion capacitor, Anode, Energy storage

Posted Date: April 20th, 2022

DOI: <https://doi.org/10.21203/rs.3.rs-1522781/v1>

License:   This work is licensed under a Creative Commons Attribution 4.0 International License.

[Read Full License](#)

Abstract

Pseudocapacitive materials with high-rate behavior of lithium-ion charge storage offer a pathway to narrow the kinetics gap with capacitive porous carbon cathode toward lithium-ion capacitors both with high energy and high power densities. However, most of pseudocapacitive materials are subject to their relatively high redox potential and/or the morphological requirement of nanoscale, thus resulting in an undesirable decrease in energy density from either gravimetric or volumetric sides. Here, we demonstrate that lithium-rich disordered rock salt vanadium oxide (DRX-Li₃V₂O₅) exhibits typical pseudocapacitive behaviors within a low working potential range between 0.1 V and 2 V versus a Li/Li⁺ reference electrode. The pseudocapacitive behaviors of DRX-Li₃V₂O₅ is inherent to its bulk form, which mainly arises upon a percolating network that offers three-dimensional lithium-ion transport pathways confirmed by the Monte Carlo simulations. A lithium-ion capacitor is further assembled by combing this pseudocapacitive DRX-Li₃V₂O₅ anode with a capacitive activated carbon cathode, yields a cell voltage of 4.0 V and both high values of energy and power densities, higher than or comparable to that of the state-of-art lithium-ion capacitors based on graphite and other pseudocapacitive materials. Lithium-ion capacitor based on this high-rate and low-cost DRX-Li₃V₂O₅ anode is ready for commercialization.

Introduction

Lithium-ion capacitors (LICs) as a new type of energy storage devices, have been proposed to possess the advanced characteristics of both batteries and supercapacitors^{1,2}. This device is expected to alleviate technological challenges associated with the rapid development of portable electronics, electric vehicles, and rail transit which are primarily relied on high and fast energy delivery systems³. Commercially available LICs are usually based on pre-lithiated graphite anode and activated carbon cathode which are separated by a porous membrane soaked in a lithium-ion based organic electrolyte⁴. LICs can deliver high energy density (twice more than conventional supercapacitors), however the delivered energy density of LICs would decrease rapidly at the high charge/discharge rates⁵. These limitations are intrinsically due to the kinetics mismatch between two electrodes, where the kinetics of battery-type graphite is far more sluggish than capacitive activated carbon³.

In the past decade, various strategies have been proposed to solve the issues of kinetics mismatch between graphite cathode and activated carbon anode for LICs. An alternative approach is to use pseudocapacitive materials to replace graphite^{3,6}. Thanks to charge storage occurs via Faradaic charge transfer at surface or near surface or channels of pseudocapacitive materials, the kinetics is not diffusion-limited and thus highly comparable to capacitive activated carbon^{7,8}. So far, several transition metal oxides and sulfides were found to exhibit pseudocapacitive behavior.⁶ With better understanding of pseudocapacitive behavior, pseudocapacitance is typically classified into two categories: intrinsic and extrinsic. Intrinsic pseudocapacitive materials exhibit the pseudocapacitive responses is inherent to the materials in its bulk form, or size and morphological independent^{6,7}. These are materials such as T-

Nb_2O_5^9 , $\text{TiO}_2(\text{B})^{10}$, and $\text{Nb}_{16}\text{W}_5\text{O}_{55}^{11}$ with large, open channels or layered structure which allow rapid ion access and significantly improved rate capability. However, these intrinsic pseudocapacitive materials worked with the relatively high redox potential (> 1 V versus Li/Li^+), thus resulting in an undesirable but necessary decrease in working potential of LICs and thus energy density. On the other hand, extrinsic pseudocapacitive materials (e.g. MoS_2^{12} , MoO_3^{13} , $\text{H}_2\text{Ti}_6\text{O}_{13}^{14}$, $\text{V}_2\text{O}_5^{15}$,) do not directly exhibit pseudocapacitive response in the bulk state, which are strongly size-dependent. So, the most effective way to achieve extrinsic pseudocapacitance is to create nanometer-sized or porous structures due to decrease Li^+ solid-state diffusion distances. However, these nanosized or porous structures inherently result in a low volumetric energy density, a low initial coulombic efficiency, and a high-cost synthesizing process.

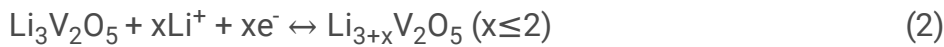
Lithium-rich disordered rocksalt (DRX) oxides possess a crystalline rock-salt structure (or NaCl-like structure) but with a cation disordering characteristic that refers to the random distribution of lithium and transition metal (TM) on the cation lattice^{16,17}. Such cation disordering structure leads to the formation of a lithium percolating network, enabling fast lithium diffusion¹⁷. Since the lithium-rich DRX oxides were found to be electrochemically active, more attention was paid to use them as the cathode materials which were capable of delivering high capacities exceeding those of commercial cathode materials^{18–20}. There have been only a few studies that investigate the lithium-ion further intercalated into lithium-rich DRX oxides as the anode material²¹. These limited results suggested that lithium-rich DRX oxides can be cycled reversibly between 0.01 V and 2.0 V accompanied by a fast $2e^-$ charge-transfer process, in the case of DRX- $\text{Li}_3\text{V}_2\text{O}_5$ ²¹. These unique features indicate that DRX- $\text{Li}_3\text{V}_2\text{O}_5$ may be an ideal pseudocapacitive material for LICs that researchers are pursuing all the time.

Here, we characterize capacitive charge storage in DRX- $\text{Li}_3\text{V}_2\text{O}_5$ and demonstrate that DRX- $\text{Li}_3\text{V}_2\text{O}_5$ is a pseudocapacitance-dominated material with an average charge/discharge potential of 0.6 V versus a Li/Li^+ reference electrode. Theoretical calculations results show that pseudocapacitive properties of DRX- $\text{Li}_3\text{V}_2\text{O}_5$ is strongly related to its unique 3D Li-ion percolation network through the 0-TM channels where TMs are absent in the face-sharing octahedra. A LIC with this pseudocapacitive DRX- $\text{Li}_3\text{V}_2\text{O}_5$ anode yields a safe cell voltage up to 4.0 V, which is close to graphite based LIC but much higher than those of other pseudocapacitive anodes based LICs. Additionally, this LICs delivers a maximum gravimetric energy density of 126.8 Wh kg^{-1} and a high gravimetric power density of $38\,520 \text{ W kg}^{-1}$ as well as a long-term cycling life over 30 000 cycles.

Results And Discussion

Lithium-rich disordered rock salt (DRX) $\text{Li}_3\text{V}_2\text{O}_5$ was achieved by electrochemical Li^+ intercalation into commercial V_2O_5 powder through a two-electrode $\text{V}_2\text{O}_5//\text{Li}$ coin-type cell^{21,22}. Figure 1a exhibits the typical voltage curve during the initial and followed lithiation/delithiation process. Several voltage plateaus are found during the initial lithiation process down to 1.0 V (versus Li/Li^+), corresponding to

irreversible phase transformations of V_2O_5 to DRX- $Li_3V_2O_5$, as confirmed by three new peaks (26.4° , 44.0° , and 64.4°) arising from ex-situ XRD patterns in Fig. 1b. The lithiation plateau below 1.0 V suggests Li^+ could further insert into DRX- $Li_3V_2O_5$. Even the lithiation potential down to 0.1 V (vs Li/Li^+), the rock-salt phase still maintains. In the followed delithiation and lithiation process, the symmetric voltage profiles are observed (Fig. S1), which indicates that DRX- $Li_3V_2O_5$ can be cycled reversibly between 0.1 and 2.0 V (vs Li/Li^+). The observed specific capacity and average discharge voltage are $\sim 220 \text{ mAh g}^{-1}$ and 0.6 V (vs Li/Li^+), respectively. Ex-situ XRD patterns shown in Fig. S2 further confirm the newly-formed rock salt phase persists throughout the followed electrochemical process and even cycled more than 1000 cycles. The initial irreversible Li^+ intercalation into V_2O_5 and the followed reversible Li^+ deintercalation/intercalation processes on $Li_3V_2O_5$ are represented by the following equation²¹:



We employed transmission electron microscopy (TEM) to disclose the structure of DRX- $Li_3V_2O_5$. Figure 1c and Fig. S3 show that the bulk of DRX- $Li_3V_2O_5$ is well crystallized. The well-resolved lattice fringes with an interplanar distance of 0.2 nm can be indexed to the (200) plane of DRX- $Li_3V_2O_5$. The corresponding electron diffraction (ED) pattern in Fig. 1d shows spots which are characteristic of a system composed of DRX- $Li_3V_2O_5$. In addition, DRX- $Li_3V_2O_5$ was coated by a thin solid electrolyte interphase layer (SEI) with a thickness of ~ 5 nm. X-ray photoelectron spectroscopy (XPS) in Fig. S4 confirmed that SEI is mainly composed by organic compounds and inorganic salts²³. SEM images in Fig. S5 show that DRX- $Li_3V_2O_5$ maintain the bulk morphology of pristine V_2O_5 powder, even after a long-term cycling process.

To investigate the charge storage mechanism during Li-ion insertion and extraction, ex-situ XPS spectra are measured at different lithiation and delithiation state, as shown in Fig. 1e. For pristine V_2O_5 , the V 2p spectrum exhibits one main peak centered at 517.4 eV, associated with V^{5+} ¹⁵. As the potential is down to 2.0 V, the V 2p peak becomes broaden and gradually shifts to lower binding energy, indicating lowered valence state of vanadium ions upon lithiation. The V 2p peak could be separated to three peaks at 515.2 eV, 516.1 eV, and 517.4 eV associated with V^{5+} , V^{4+} and V^{3+} , respectively²². Upon discharge at 1.0 V (vs Li/Li^+), negligible change is occurred on V 2p peak except the relative fractions of V^{5+} is reduced slightly (Fig. S6). As the potential down to 0.1 V (vs Li/Li^+), the broaden V 2p peaks gradually shifts to lower binding energy, suggesting the formation of V^{2+} ions (at 513.6 eV) in $Li_{3+x}V_2O_5$. After the potential returns to 2.0 V (vs Li/Li^+), V 2p slightly shifts to higher bonding energy, accompanying with the disappearance of V^{2+} ions and the decrease of the relative fractions of V^{3+} ions as well as the increase of the relative fractions of V^{4+} and V^{5+} . The V 2p XRS spectra (Fig. S7) for the electrode discharged to 0.1 V (vs Li/Li^+) in the second cycle and tenth cycle overlap with the spectra in the first cycle, indicating that the V redox is highly reversible. A previous V K-edge X-ray absorption near edge structure (XANES) spectra showed that

DRX- $\text{Li}_3\text{V}_2\text{O}_5$ predominantly consists of V^{3+} and V^{4+} ; lithiation reduces V^{4+} to V^{3+} or even lower than V^{3+} ²¹. The ex-situ XPS studies carried out here confirm that lithiation/delithiation results in a continuous and reversible change in oxidation state of V. Besides V 2p, reversible changes of Li 1s, O 1s and F 1s upon lithiation/delithiation were observed in Fig. S8, which are indicative of reversible lithiation-delithiation in DRX- $\text{Li}_3\text{V}_2\text{O}_5$.

To elucidate the Li^+ diffusion mechanism in DRX- $\text{Li}_3\text{V}_2\text{O}_5$, density functional theory (DFT) calculations using a cluster expansion (CE) model and Monte Carlo (MC) simulations were performed. Figure 2a depicted the typical DRX structure of $\text{Li}_3\text{V}_2\text{O}_5$ where O anions fully occupy the 4a sites in the anionic sublattice, while Li and V cations distribute randomly at the octahedral 4b sites in the cationic sublattice. In a DRX material, Li diffusion proceeds by hopping from one octahedral site to another octahedral site via an intermediate tetrahedral site¹⁹. The most relevant to Li transport is through tetrahedral clusters (formed by O anions) including 0-TM, 1-TM, and 2-TM, as shown in Fig. 2b. Especially, 0-TM channels (or Li_4 tetrahedra) are considered as the most important for fast Li transport because of that 0-TM channels can form a percolating network to support macroscopic lithium diffusion²⁴⁻²⁷. To model the realistic condition, a CE model (more details seen in experimental part and Fig. S9) in the configurational space of $\text{Li}_x\text{V}_{5-x}\text{O}_5$ ($x=3$) on a rocksalt lattice was constructed to enable extensive configurational sampling to determine the system energy. MC simulations were then performed to evaluate the equilibrium ordering in the multicomponent compounds, which could further analyze the local and macroscopic Li-transport environments in $\text{Li}_x\text{V}_{5-x}\text{O}_5$. Figure 2c shows the calculated Li concentrations in tetrahedral clusters which can be used to study the connectivity based on CE-MC-derived structures. All the fractions of Li content of 0-TM, 1-TM and 2-TM tetrahedral clusters are more than 88% of the total number, indicating a uniform distribution of Li throughout the MC supercell without a tendency for Li or V sites aggregation. While the number of Li_4 tetrahedra is critical for local Li migration, sufficient connectivity between these environments is another key criterion to ensure macroscopic Li transport. To visualize the Li diffusion pathways in DRX- $\text{Li}_3\text{V}_2\text{O}_5$, representative MC structures at 300 K are depicted in Fig. 2d. A 3D framework of 0-TM connected Li networks (highlighted in green color) in $\text{Li}_3\text{V}_2\text{O}_5$ is formed with a short-range order structure. Note that short-range order strongly modifies the population of local Li_4 tetrahedral clusters which will lead to a fast Li transport. The slices in Fig. 2d provide more details on the interconnected skeleton-like pathways, showing the excellent connectivity of Li-migration channels. The connectivity of 1-TM, 2-TM, and 3-TM in the same structure is also studied (Fig. S10), which demonstrates that 1-TM and 2-TM have a large number of channels for Li^+ diffusion. From the simulated results presented above, the pathways of Li transfer in $\text{Li}_3\text{V}_2\text{O}_5$ becomes clear. The 3D framework of 0-TM channels forms a fast transfer pathway in the whole crystal, like the highway, which will lead to a fast Li^+ redistribution macroscopically; the uniform distribution of 1-TM and 2-TM makes sure that Li^+ could reach every corner of crystal.

To probe the structures and electronic properties (band structure and density of state, DOS) during the Li-inserted process including $\text{Li}_3\text{V}_2\text{O}_5$ (initial structure), $\text{Li}_4\text{V}_2\text{O}_5$ (transition structure) and $\text{Li}_5\text{V}_2\text{O}_5$ (fully

lithiated structure) have been simulated by DFT calculations using the PBE+U functional were performed (see Experimental section for details) on different Li/V ordering in a $\sqrt{5}\times\sqrt{5}\times 2$ supercell which contains $2x$ Li (x is the Li number in the unit cell), four V and ten O atoms. For $\text{Li}_3\text{V}_2\text{O}_5$, a typical lamellar structure can be observed, which could be divided into V-O slab and Li slab along the b direction (Fig. S11). The asymmetric spin-up and spin-down DOS indicates $\text{Li}_3\text{V}_2\text{O}_5$ crystal is a ferromagnetic material, which agrees with the previous study.²¹ Both $\text{Li}_4\text{V}_2\text{O}_5$ and $\text{Li}_5\text{V}_2\text{O}_5$ crystals have also a typical lamellar structure (Fig. S11). As predicted, the thickness of lamella gradually increases with the increase of Li content (from 6.8 Å ($\text{Li}_3\text{V}_2\text{O}_5$) to 6.9 Å ($\text{Li}_4\text{V}_2\text{O}_5$) and finally reached 8.1 Å ($\text{Li}_5\text{V}_2\text{O}_5$) in b direction). Interestingly, the lattice vector in the b direction hardly changes for transition structure. But in plane a and c , a large lattice distortion (9.2%) has been observed even larger than $\text{Li}_5\text{V}_2\text{O}_5$ crystal (6.2%), suggesting a relatively strong Li-O interaction in $\text{Li}_4\text{V}_2\text{O}_5$. Note that the band structure of DRX- $\text{Li}_3\text{V}_2\text{O}_5$ does not change significantly with the increase of Li content. DRX- $\text{Li}_3\text{V}_2\text{O}_5$ is a narrow gap semiconductor with an indirect bandgap of 0.94 eV (Fig. 2e). The indirect bandgap increases to 1.22 eV for DRX- $\text{Li}_4\text{V}_2\text{O}_5$ and then decreases to 0.78 eV for DRX- $\text{Li}_5\text{V}_2\text{O}_5$. The larger bandgap of DRS- $\text{Li}_4\text{V}_2\text{O}_5$ can be explained by the fact that the relatively large lattice distortion localized the valence electron of Li, while larger Li concentration suggest more delocalized Li electron gas, thus leading to a smaller bandgap of DRS- $\text{Li}_5\text{V}_2\text{O}_5$. These structural and theoretical studies emphasize the potential value of a percolating network to enable rapid ion transport within the semiconducting DRX- $\text{Li}_5\text{V}_2\text{O}_5$.

To investigate the potential phenomenon of intercalation pseudocapacitance and high-rate behavior of DRX- $\text{Li}_3\text{V}_2\text{O}_5$ electrode, several classical electrochemical techniques were carried out. Figure 3a shows the potential response of thin DRX- $\text{Li}_3\text{V}_2\text{O}_5$ electrode during the galvanostatic intermittent titration technique (GITT) test. The potential profile is pseudolinear, which are clearly distinguish this charge storage mechanism from battery-type or diffusion dominated charge storage⁹. The polarization between the charge/discharge curve is relatively small ($\Delta E = \sim 0.15$ V). The lithium-ion storage is mainly below 1.0 V with an average working potential of ~ 0.6 V, which is much lower than that of Li insertion in other high-rate electrodes, such as Nb_2O_5 (~ 1.6 V)⁹, $\text{TiO}_2\text{-B}$ (1.5 V)¹⁰, and LTO (1.55 V)²⁸, thus enabling a LIC with higher working potential. The D_k value can be calculated by solving Fick' second law based on the GITT potential curves, shown in Fig. S12. The average Li^+ diffusion coefficients are determined to be at the level of $1.15\times 10^{-13}\sim 1.18\times 10^{-12}$ $\text{cm}^2 \text{ s}^{-1}$, suggesting the fast Li^+ diffusion in DRX- $\text{Li}_3\text{V}_2\text{O}_5$ anode.

Cyclic voltammetry (CV) measurements were employed to gain insight into the reaction kinetics and charge-storage mechanism of the DRX- $\text{Li}_3\text{V}_2\text{O}_5$ electrode. Figure 3b and Fig. S13 show the CV curves from 0.2 to 100 mV s^{-1} in a thin electrode where it is evident that similar shapes with broad peaks during both anodic and cathodic process. The broad redox peaks suggest that DRX- $\text{Li}_3\text{V}_2\text{O}_5$ electrode mainly store charge via an intercalation dominant process with respect to bulk DRX- $\text{Li}_3\text{V}_2\text{O}_5$ with limited surface area. These anodic peaks show small shift ($\Delta E = \sim 0.1$ V) as the scan rate increases from 0.2 to 10 mV s^{-1} (Fig. 3c), suggesting small polarization at high rates. Above a critical sweep rate of 10 mV s^{-1} , the peaks

shift increased more rapidly as the cell reaches diffusion-limited behavior. According to the power law between the peak currents (i) and scan rates (ν)⁹:

$$i = a\nu^b \quad (1)$$

where a and b are appropriated values. Previous studies proposed that the b -value of 1 indicates a capacitive behavior where the kinetics are surface-controlled, whereas the b -value of 0.5 represents a battery-like behavior where the kinetics are diffusion-controlled^{9,29}. Then, plots of $\log(\nu)$ - $\log(i)$ are depicted in Fig. 3d. The b -values of for anodic and cathodic peaks are 0.85 and 0.87 within a sweep rate range from 0.2 to 10 mV s^{-1} (corresponding to charge time > 200 s), respectively, indicating that the kinetics are mainly surface-controlled, thus capacitive-dominated⁹. A change in the slope occurred as the scan rates above 10 mV s^{-1} , corresponding to a decrease in b -value to 0.69 for anodic peaks, respectively. Such rate limitation arisen from diffusion constraints at high sweep rates was observed in other pseudocapacitive materials such as Nb_2O_5 ^{9,29}, and TiO_2 ¹⁰ which can be attributed to the diffusion constraints/limitations or an increase of the Ohmic contribution.

The relationship between capacity and scan rate can also establish to investigate the electrochemical lithiation/delithiation kinetics of DRX- $\text{Li}_3\text{V}_2\text{O}_5$. Fig. S14 depicts the plot of capacity versus $\nu^{1/2}$ shows that the capacity does not vary significantly as the scan rate increases from 0.2 to 100 mV s^{-1} . This indicates that solid-state lithium-ion diffusion is not the rate-limiting step for charge storage, thus capacitive dominated mostly.^{6,9} While as the scan rate over 10 mV s^{-1} , the capacity decreases rapidly upon the increase of scan rate, approximate a linear relationship. This indicates a rate-limited diffusion process at high sweep rates.

A previous study reported by Dunn et al. suggest that the measured current response at a fixed potential is composed of both capacitive currents (expressed as $k_1\nu$) and diffusion-controlled currents ($k_2\nu$), as given in followed equation^{9,29}:

$$i(V) = k_1\nu + k_2\nu^{1/2}$$

where i is current at a particular potential, ν is scan rate, k_1 and k_2 are fitting parameters. Accordingly, the contribution of capacitive response can be evaluated by $k_1\nu/i$. Figure 3e shows the typical voltage profile for the capacitive currents (shade area) of DRX- $\text{Li}_3\text{V}_2\text{O}_5$ electrode as comparted with the total measured currents at the scan rate of 1 mV s^{-1} . The capacitive charge is mainly generated at around the peak voltage, and the corresponding capacitive contribution is qualified as 82% of the total current. That is to say that most of charge storage is capacitive throughout the entire voltage range measured, which indicates that DRX- $\text{Li}_3\text{V}_2\text{O}_5$ electrode is pseudocapacitive in nature during the lithiation/delithiation process. The kinetics analysis reveals that the high proportion of diffusion-controlled currents are found on either side of 0.6 V (vs Li/Li^+) in the lithiation process. Reports have suggested that the initial insertion of Li leads to an increase in tetrahedral site occupancy with a constant Li occupancy in the octahedral

sites, while $x \geq 1$ of Li inserted into $\text{Li}_{3+x}\text{V}_2\text{O}_5$ (lithiation potential ≤ 0.5 V) induces a redistribution of Li where a sharp decrease in octahedra site occupancy and a linear increase in Li tetrahedra sites occupancy²¹. This transition on Li site occupancy may influence the kinetics of Li ion diffusion.

Electrical impedance spectroscopy (EIS) measurements were conducted to confirm the pseudocapacitive characteristic of Li ion charge storage for DRX- $\text{Li}_3\text{V}_2\text{O}_5$ electrode. The Nyquist plot measured at 0.2 V (vs Li/Li⁺) in Fig. 3f consist of two parts: a semicircle line in the high frequency and an oblique straight line in the low frequency, corresponding to the charge transfer resistance and diffusion resistance, respectively^{7,30}. Interestingly, in the low frequency region, the angle between the oblique line with Z-axis is approximately close to 90°, which indicates that the Li ion charge storage in DRX- $\text{Li}_3\text{V}_2\text{O}_5$ electrode is not limited by diffusion process⁷. This surface-controlled behavior is well retained for thick electrodes with the mass loadings of 2, 6 and 8 mg (Fig. S15). For thick electrodes, the large proportions of the capacitive process are also maintained (Fig. S16), e.g., 74% for 2 mg-mass-loading electrode and 68% for 8 mg-mass-loading electrode at 1 mV s⁻¹.

Figure 4a displays the typical galvanostatic charge-discharge voltage profiles over DRX- $\text{Li}_3\text{V}_2\text{O}_5$ electrode under a wide current density range from 0.1 A g⁻¹ to 20 A g⁻¹ in the potential window 0.1-2.0 V (vs Li/Li⁺). All the charge and discharge curves are a feature like a pseudolinear in the full work potential range, which is similar to other pseudocapacitive materials, such as Nb_2O_5 ⁹, TiO_2 ¹⁰, $\text{H}_2\text{Ti}_6\text{O}_{13}$ ¹⁴. DRX- $\text{Li}_3\text{V}_2\text{O}_5$ electrode shows a superior rate performance (Fig. 4b). At 0.1 A g⁻¹, DRX- $\text{Li}_3\text{V}_2\text{O}_5$ anode delivers a specific capacity of 212.4 mAh g⁻¹. Even at the high rate of 5 and 20 A g⁻¹, the specific capacity of DRX- $\text{Li}_3\text{V}_2\text{O}_5$ anode remains at 131.4 and 75.9 mAh g⁻¹, 61.9% and 35.7% of initial specific capacity, respectively. In comparison, the rate performance for DRX- $\text{Li}_3\text{V}_2\text{O}_5$ is significantly higher than battery-like graphite³¹ and $\text{Li}_4\text{Ti}_5\text{O}_{12}$ ³² and highly comparable to other pseudocapacitive materials (Fig. 4c), such as $\text{Li}_2\text{TiSiO}_5$ nanoparticles³³, 2D MXene³⁴, Nb_2O_5 ^{9,35}, $\text{TiO}_2(\text{B})$ nanowires³⁶, meso- MoS_2 ³⁷, and $\text{H}_2\text{Ti}_6\text{O}_{13}$ nanowires³⁸. It should be pointed out that such high-rate performance of DRX- $\text{Li}_3\text{V}_2\text{O}_5$ has been achieved without create nanometer-sized or porous structures. To examine the size effect on rate capability, a DRX- $\text{Li}_3\text{V}_2\text{O}_5$ nanosheet electrode was achieved by a nanosheet-morphological V_2O_5 precursor through the same lithiation process (Fig. S17), as confirmed by ex-situ XRD patterns in Fig. S18. Figure S19 shows that the specific capacity and rate capability of DRX- $\text{Li}_3\text{V}_2\text{O}_5$ nanosheets electrode do not obtain significantly improvement as compared with bulk electrode. Furthermore, DRX- $\text{Li}_3\text{V}_2\text{O}_5$ bulk electrode (Fig. 4d) exhibits excellent cycling stability even after no 2000 cycles at the different rates of 2 A g⁻¹ and 10 A g⁻¹. During the whole cycling test, the corresponding Coulombic efficiencies are close to 100%. The excellent cycling performance can be attributed to that the stable structure and morphology for DRX- $\text{Li}_3\text{V}_2\text{O}_5$ as confirmed by ex-situ XRD patterns (Fig. S2) and SEM images (Fig. S5).

The above results present that DRX- $\text{Li}_3\text{V}_2\text{O}_5$ electrode exhibits typical electrochemical features of a pseudocapacitive material despite Li ion charge storage occurring in the bulk. It's pointed out that such

behavior is highly consistent with intercalation pseudocapacitance. This is because of those indicatively electrochemical features are observed such as currents that are linearly proportional to the sweep rate, CV peaks that are broad with small peak-to-peak voltage separation, capacity that does not decay rapidly with charging rate, and the angle between the oblique line with Z-axis that is approximately close to 90° . In addition, the pristine rock-salt structure does not undergo phase transformations on insertion during the constant lithiation/delithiation process, which is considered as a key design rule for intercalation pseudocapacitance. Most importantly, facile three-dimensional (3D) lithium-ion diffusion through a percolating network of octahedron-tetrahedron-octahedron pathways is crucial.

To further identify the potential of pseudocapacitive DRX- $\text{Li}_3\text{V}_2\text{O}_5$ in LICs, a prototype full cell was fabricated by using DRX- $\text{Li}_3\text{V}_2\text{O}_5$ as pseudocapacitive negative electrode and home-made polyaniline derived porous carbon (PDPC) as capacitive-type positive electrode in LiFP_6 based organic electrolyte, as schematically illustrated in Figure 5a. More details about the synthesis of PDPC cathode can be seen in our previous work^{39,40}. This DRX- $\text{Li}_3\text{V}_2\text{O}_5$ //PDPC LIC was cycled upon a cell voltage window ranging in 1.0-4.0 V with an optimal negative/positive electrode mass ratio of 1:1 (Fig. S20). Figure 5b and Fig. S21 shows the CV curves of DRX- $\text{Li}_3\text{V}_2\text{O}_5$ //PDPC LIC under a scan rate range between 5 and 100 mV s^{-1} . The CV profile of this LIC shows a slight deviation from the ideal rectangular CV shape of symmetric supercapacitor, which is mainly associated to the synergistic effect of two different energy-storage mechanisms (pseudocapacitance for anode and EDLC for cathode)⁴¹.

DRX- $\text{Li}_3\text{V}_2\text{O}_5$ //PDPC LIC was further cycled galvanostatically, while monitoring the cell voltage and recording the potentials of the positive and negative electrodes separately vs. a Li reference electrode through a Swagelok cell. Figure 5c shows the typical galvanostatic charge/discharge profiles at a current density of 0.2 A g^{-1} in the potential range between 1 V and 4 V. In this range, the PDPC cathode works within 4.32-2.27 V vs Li/Li^+ , which prevents SEI formation on the surface of porous carbon and avoids electrolyte oxidation. While the DRX- $\text{Li}_3\text{V}_2\text{O}_5$ negative electrode operates within 0.32-1.27 V versus Li/Li^+ , avoiding lithium plating. Concerning the high rates, no sign of electrolyte decomposition and Li plating occur (Fig. S22), as confirmed by the working potential ranges for DRX- $\text{Li}_3\text{V}_2\text{O}_5$ and PDPC electrodes within safe area.

Figure 5d and Fig. S23 shows that the galvanostatic charge/discharge curves under the different rates exhibit approximately linear slope under the wide range of current densities, presenting a typical electrochemical characteristic of hybrid capacitors. The specific capacities (Fig. 5e) of DRX- $\text{Li}_3\text{V}_2\text{O}_5$ //PDPC LIC (expressed per total mass of both electrodes) were calculated with the value of 56.9, 45.5, 38.4, 32.4, 24.1, 20.6, 17.1, 16.2 mAh g^{-1} at the current densities of 0.1, 0.5, 1, 2, 5, 10, 15, 20 A g^{-1} , respectively. The energy density and power density of DRX- $\text{Li}_3\text{V}_2\text{O}_5$ //PDPC LIC were further evaluated from charging/discharging curves, as plotted in Fig. 5f. At a gravimetric power density of 184.0 W kg^{-1} , the LIC delivers a high gravimetric energy density of 126.8 Wh kg^{-1} . Even at an ultrahigh gravimetric power density of 38 520 W kg^{-1} , the LIC can still deliver 21.4 Wh kg^{-1} . The power density of DRX-

$\text{Li}_3\text{V}_2\text{O}_5//\text{PDPC}$ LIC is on the same level as the conventional supercapacitors, while the energy density of this LIC is 2-3 orders of magnitude higher than that of conventional supercapacitors¹. The Ragone plot also shows that the energy and power densities of this LIC outperforms many the state-of-art reported LICs, including battery-like anodes based LICs (such as graphite//AC⁵, $\text{Li}_4\text{Ti}_5\text{O}_{12}$ //AC⁴²) and pseudocapacitive anodes based LICs (such as $\text{T-Nb}_2\text{O}_5//\text{AC}$ ⁴³, $\text{TiO}_2\text{-rGO}$ //AC⁴⁴, $\text{H}_2\text{Ti}_6\text{O}_{13}$ //AC¹⁴, MXene//AC⁴⁵).

Most importantly, this LIC exhibits the extremely stable cycling life. Figure 5g shows that even after 20,000 constant current charge/discharge cycles at a current density of 2 A g^{-1} , 80.1% of its capacity was retained. The coulombic efficiencies of DRX- $\text{Li}_3\text{V}_2\text{O}_5//\text{PDPC}$ LIC are approximate 100% during the whole cycling. Even at a high current density of 5 A g^{-1} , this LIC has no obvious decay (retention ratio: 85.6%) after 30,000 cycles (Fig. S24). In addition, three-electrode Swagelok cell was used to monitor the potential changes of respective negative and positive electrodes during long-term cycling. The up and down potentials in Fig. S25 for DRX- $\text{Li}_3\text{V}_2\text{O}_5$ and PDPC are in stable area, suggesting no sign of electrolyte decomposition and Li plating during the cycling. The capacity decay of this LIC is mainly caused by the capacity decay of DRX- $\text{Li}_3\text{V}_2\text{O}_5$ negative electrode during the long-term cycles, which is indicative by the expanded potential swing window of DRX- $\text{Li}_3\text{V}_2\text{O}_5$ negative electrode and the decreased potential swing window of PDPC positive electrode. For a LIC, the charge of Li^+ inserted into negative electrode should counter-balance the charge of positive electrode.⁴⁶ Once the Li^+ stored in the charged DRX- $\text{Li}_3\text{V}_2\text{O}_5$ negative electrode becomes inefficient to fully counter-balance the charge of PDPC positive electrode, the swing window of PDPC positive electrode will decrease during the subsequent cycling. Overall, the above results suggest that pseudocapacitive DRX- $\text{Li}_3\text{V}_2\text{O}_5$ anode with unique 3D Li^+ diffusion path shows the great potential for next-generation LICs with low cost to replace commercial graphite, LTO and other pseudocapacitive materials.

Conclusions

In summary, we have demonstrated that DRX- $\text{Li}_3\text{V}_2\text{O}_5$ has the pseudocapacitive characteristics during lithium-ion intercalation: the little structural change during intercalation process, the absence of solid-state diffusion limitation, the broad redox peaks with small voltage offsets even at high rates, and the sloping charging/discharging curves. The pseudocapacitive behavior of DRX- $\text{Li}_3\text{V}_2\text{O}_5$ is achieved without nanoscaling by its disordered rock-salt crystal structures which has a percolating network that offers three-dimensional lithium-ion transport pathways, as confirmed by MD calculations. DRX- $\text{Li}_3\text{V}_2\text{O}_5$ has a relatively low working potential range, enabling a LIC with high working potential up to 4 V, which is close to that of graphite based LICs and much higher than that of high-rate $\text{Li}_4\text{Ti}_5\text{O}_{12}$ and other pseudocapacitive materials of $\text{T-Nb}_2\text{O}_5$ and $\text{TiO}_2\text{-B}$ based LICs. Furthermore, DRX- $\text{Li}_3\text{V}_2\text{O}_5$ anode based LIC can deliver both high energy and power densities as well as long-term cycling stability. To best our knowledge, this is first LICs based on lithium-rich disordered rock salt metal oxide materials. Taken together, this work thus establishes lithium-rich disordered rock salt metal oxides as a new family of

pseudocapacitive materials that allow as-fabricated LIC to make significant improvement in cell voltage and power density while still maintain their high-energy density advantage, thus opening a new avenue for high-rate energy storage devices.

Methods

Materials:

All chemicals were of analytical grade and used directly without any purification. V_2O_5 (AR, 99.0%), 1-Methyl-2-pyrrolidinone (NMP, AR, $\geq 99.9\%$) were purchased from Aladdin Chemicals. Polyvinylidene fluoride (PVDF), acetylene black and Li foil were purchased from MTI corporation. 1 M $LiPF_6$ in EC:DMC:EMC = 1:1:1 Vol% was purchased from DoDoChem, China.

Fabrication of half-cell and hybrid Devices:

For the fabrication of DRX- $Li_3V_2O_5$ bulk anode, V_2O_5 (AR, 99.0%) active material, acetylene black (as the conducting filler), and polyvinylidene fluoride (PVDF) (as the binder) with a mass ratio of 5:4:1 in methyl-2-pyrrolidone (NMP) were mixed in a mortar. The well-mixed slurry was homogeneously coated on the copper foil using a film casting doctor. After heated at 110 °C for 10 h under vacuum, the film was pressed at 10 MPa and then punched into 12 mm diameter round electrodes with a mass loading of about 2 mg. In order to study the kinetic mechanism of DRX- $Li_3V_2O_5$ anode, the thin electrode with a mass loading of 0.4 mg and thick electrodes with the mass loadings of 6 and 8 mg were prepared with same procedure. V_2O_5 nanosheets were synthesized according to previous work⁴⁷, which were used to obtain the DRX- $Li_3V_2O_5$ nanosheet anode through the same procedure with bulk-morphological anode.

For the cathode materials, high-performance polyaniline derived porous carbon (PDPC) was synthesized according to our previous report.³⁹ 90 wt% PDPC and 10 wt% polytetrafluoroethylene (PTFE) were mixed and then were rolled into thin sheets. After heated at 80 °C for 10 h, the sheet was cut into 10 mm × 10 mm electrodes, and then pressed on Al foil at 10 MPa. After that, the PDPC cathode electrodes were dried over-night at 160 °C under vacuum and then were transferred into glove box filled with Ar.

For half cells, the anode was tested using the coin type cell (2032 type), where Celgard 2400 was used as the separator, and Li metal foil was used as the counter and reference electrode. The cells were cycled under a potential window of 0.1-2 V (Li/Li⁺). Before the fabrication of LICs hybrid cells (or full cells), the anode was charged-discharged for 5 cycles and ending in a lithiation state at 0.1 V under a current density of 0.1 A g⁻¹ in a half cell, and then detached in an Ar filled glovebox. The pre-activated anode coupled with a home-made polyaniline derived porous carbon (PDPC) cathode was assembled in a 2032 type coin cell, which was separated by a round Celgard 2400. For both half and full cells, 1 M $LiPF_6$ in EC:DMC:EMC = 1:1:1 Vol% was employed as the electrolyte. The half/full cells were assembled into Ar filled glovebox with the low H₂O and O₂ contents (less than 0.1 ppm).

Structural characterization: Field emission scanning electron microscopy (FESEM, JSM-7800F, JEOL, Japan) and transmission electron microscopy (TEM, Tecnai F20) were carried out to investigate the morphology and structure of as-prepared samples. The structure and composition of the samples was studied by Powder X-ray diffraction (XRD, Rigaku D/Max-2400, Japan) using Cu-K α radiation. X-ray photoelectron spectroscopy (XPS, Perkin-Elmer PHI-5702 Spectrometer) was used to record the surface chemical species of the samples. For the ex-situ XRD/XPS characterizations, the assembled half-cells were cycled with potential window between 0.1-2 V, then the DRX-Li $_x$ V $_2$ O $_5$ electrodes under the different lithiated state were obtained by disassembling the cells into Ar filled glovebox. The electrodes were washed with dimethyl carbonate (DMC) to remove residual electrolytes. In order to avoid the XRD signal interference and acquire the strong XRD signal, a thick V $_2$ O $_5$ (> 10 mg cm $^{-2}$) was coating on carbon paper (Toray, TGP-H-060, Japan) current collector instead of copper foil. During the ex-situ XPS characterization, DRX-Li $_{3+x}$ V $_2$ O $_5$ electrodes were etched by Ar $^+$ for 100 s with a etch rate of 0.29 nm/s to remove the surface SEI layer.

Electrochemical Measurements:

Cyclic voltammetry (CV) test, galvanostatic charge/discharge measurements and electrical impedance spectroscopy (EIS) test were recorded by a CHI760E (Shanghai, China). Life-span tests for half-cell and hybrid cells used a battery test system (Land CT2001A model, Wuhan Land Electronics, Ltd.). The energy density (E , Wh kg $^{-1}$) of hybrid LICs can be evaluated by the constant discharge current (I), the cell voltage (V) and the start and end-of-discharge time (t_1 and t_2) according to the following equation:

$$E = \int_{t_1}^{t_2} IV dt$$

The power density (P , W kg $^{-1}$) of hybrid LICs can be achieved by the energy density (E) and the discharging time (t) according to the following equation:

$$P = E/t$$

Computational details

All the density functional theory (DFT) calculations with collinear spin-polarization were performed by the Vienna ab initio simulation package (VASP) using the projector augmented wave (PAW) method^{48,49}. The generalized gradient approximation (GGA) in the Perdew-Burke-Ernzerhof (PBE) formulation with a Hubbard U extension (U value) of 3.25 eV for vanadium was adopted for structural relaxations and energy calculations^{50,51}. The plane wave energy cutoff was set as 520 eV for the plane-wave expansions. The total energy convergence criterion was 10 $^{-5}$ eV/cell, and force components were relaxed to 0.02 eV/Å. The convergence of the results with respect to these parameters has been carefully checked.

For band structure and density of states calculations of $\text{Li}_3\text{V}_2\text{O}_5$, a K-point grid of $11 \times 8 \times 12$ was used in a $\sqrt{5} \times \sqrt{5} \times 2$ supercell of the rock salt primitive cell. Different occupancies were generated, and the lowest energy structure was selected for further electronic structure analysis. Band structure and density of states visualization employed the sumo package⁵². For cluster expansion training, the unit cells of all structures were optimized with k-points per reciprocal atom (KPPRA) of 5000. The Γ -centered k-point grids for the Brillouin zone integrations were then determined automatically by KPPRA and the number of atoms⁵³. After the structure was relaxed, a static energy calculation was performed with the tetrahedron method with Blöchl corrections for more accurate total energy values.

The determination of the crystal configurations with random occupation (like $\text{Li}_x\text{V}_{5-x}\text{O}_5$) requires thousands or even more atoms, which makes it impractical to utilize the DFT simulation because of too much expensive computational cost. The CE method based on Ising model is widely used for the Hamiltonian calculation of different configurations on a parent lattice⁵⁴, which is defined by the energy associated with any distribution of atoms on the lattice. The occupation of each spin over the lattice sites of a structure represents configuration. The formalism of CE parameterizes the total energy of a structure as a linear combination of interactions between different clusters (Eq. 3).

$$E(\sigma) = \sum_{\alpha} m_{\alpha} J_{\alpha} \langle \prod_{i \in \alpha'} \sigma_i \rangle \quad (3)$$

$E(\sigma)$ is the total energy of the system with configuration σ ; α denotes a particular cluster, m_{α} is the cluster multiplicity, J_{α} is the effective cluster interaction (ECI) of that cluster, and $\langle \dots \rangle$ is the cluster correlation function⁵⁵. The energies of DFT calculations are collected and fitted in CE method. As the internal database of structures grow, the clusters set grows accordingly and then the energy of any configuration can be easily and rapidly calculated by Eq. 3. Although these models are performed on a rigid lattice, the atomic relaxations are effectively incorporated in the effective cluster interactions using relaxed configurations for fitting training⁵⁶.

For the $\text{Li}_x\text{V}_{5-x}\text{O}_5$ system, the lattice can be occupied by Li or V. We fit the cluster expansion model consisting of pair interactions up to 12.7 Å, triplet interactions up to 6.0 Å and quadruplet interactions up to 5.2 Å based on the rocksalt structure. The CE model was constructed by fitting to around 304 lattice configurations and their DFT calculated energies. In this work, the *maps* code in the alloy theoretic automated toolkit (ATAT) was adopted to generate the energy landscape and perform the CE fits. The accuracy was determined by the leave-one-out cross-validation score (LOOCV). The LOOCV is 0.052 eV/atom, indicating good fitting and prediction performances.

All canonical Monte Carlo simulations based on converged CE were performed using *emc2* in ATAT^{57,58}. To ensure the convergence of the Li network size, $15 \times 15 \times 15$ supercells of the MC configurations containing 3375 active sites totally were used. For the connectivity analysis, the number of transition

metal (TM) ions within the environment (i.e., 0-TM, 1-TM, or 2-TM channels) were used^{59,60}. The annealing simulations were started from high temperatures (2000 K) and gradually approached room temperature (300 K) with the step of 50 K, to make sure that the most stable arrangement can be obtained. Equilibrium was reached once the standard deviation in energy during each canonical MC calculation was less than 10^{-5} eV/atom. About 20 different initial structures have been simulated to ensure the convergence under every temperature to ensure the convergence.

Declarations

Acknowledgements

This work was supported by National Natural Science Foundation of China (No. 51902188), Natural Science Foundation of Jiangsu Province (No. BK20190207).

References

1. Naoi, K., Ishimoto, S., Miyamoto, J. & Naoi, W. Second generation 'nanohybrid supercapacitor': Evolution of capacitive energy storage devices. *Energy Environ. Sci.* **5**, 9363–9373 (2012).
2. Ding, J., Hu, W., Paek, E. & Mitlin, D. Review of hybrid ion capacitors: From aqueous to lithium to sodium. *Chem. Rev.* **118**, 6457–6498 (2018).
3. Simon, P. & Gogotsi, Y. Perspectives for electrochemical capacitors and related devices. *Nat. Mater.* **19**, 1151–1163 (2020).
4. Jeżowski, P. *et al.* Safe and recyclable lithium-ion capacitors using sacrificial organic lithium salt. *Nat. Mater.* **17**, 167–173 (2018).
5. Khomenko, V., Raymundo-Piñero, E. & Béguin, F. High-energy density graphite/AC capacitor in organic electrolyte. *J. Power Sources* **177**, 643–651 (2008).
6. Choi, C. *et al.* Achieving high energy density and high power density with pseudocapacitive materials. *Nat. Rev. Mater.* **5**, 5–19 (2020).
7. Augustyn, V., Simon, P. & Dunn, B. Pseudocapacitive oxide materials for high-rate electrochemical energy storage. *Energy Environ. Sci.* **7**, 1597–1614 (2014).
8. Fleischmann, S. *et al.* Pseudocapacitance: from fundamental understanding to high power energy storage materials. *Chem. Rev.* **120**, 6738–6782 (2020).
9. Augustyn, V. *et al.* High-rate electrochemical energy storage through Li^+ intercalation pseudocapacitance. *Nature Mater.* **12**, 518–522 (2013).

10. Zukalová, M., Kalbáč, M., Kavan, L., Exnar, I. & Graetzel, M. Pseudocapacitive lithium Storage in $\text{TiO}_2(\text{B})$. *Chem. Mater.* **17**, 1248–1255 (2005).
11. Griffith, K. J., Wiaderek, K. M., Cibir, G., Marbella, L. E. & Grey, C. P. Niobium tungsten oxides for high-rate lithium-ion energy storage. *Nature* **559**, 556–563 (2018).
12. Cook, J. B. *et al.* Mesoporous MoS_2 as a Transition metal dichalcogenide exhibiting pseudocapacitive Li and Na-Ion charge storage. *Adv. Energy Mater.* **6**, 1501937 (2016).
13. Brezesinski, T., Wang, J., Tolbert, S. H. & Dunn, B. Ordered mesoporous $\alpha\text{-MoO}_3$ with iso-oriented nanocrystalline walls for thin-film pseudocapacitors. *Nature Mater.* **9**, 146–151 (2010).
14. Wang, Y., Hong, Z., Wei, M. & Xia, Y. Layered $\text{H}_2\text{Ti}_6\text{O}_{13}$ -Nanowires: a new promising pseudocapacitive material in non-aqueous electrolyte. *Adv. Funct. Mater.* **22**, 5185–5193 (2012).
15. Sathiya, M., Prakash, A. S., Ramesha, K., Tarascon, J. & Shukla, A. K. V_2O_5 -anchored carbon nanotubes for enhanced electrochemical energy storage. *J. Am. Chem. Soc.* **133**, 16291–16299 (2011).
16. Clément, R. J., Lun, Z. & Ceder, G. Cation-disordered rocksalt transition metal oxides and oxyfluorides for high energy lithium-ion cathodes. *Energy Environ. Sci.* **13**, 345–373 (2020).
17. Chen, D., Ahn, J. & Chen, G. An overview of cation-disordered lithium-excess rocksalt Cathodes. *ACS Energy Lett.* **6**, 1358–1376 (2021).
18. Lun, Z. *et al.* Cation-disordered rocksalt-type high-entropy cathodes for Li-ion batteries. *Nat. Mater.* **20**, 214–221 (2021).
19. Lee, J. *et al.* Unlocking the potential of cation-disordered oxides for rechargeable lithium batteries. *Science* **343**, 519–522 (2014).
20. Kan, W. H. *et al.* Understanding the effect of local short-range ordering on lithium diffusion in $\text{Li}_{1.3}\text{Nb}_{0.3}\text{Mn}_{0.4}\text{O}_2$ single-crystal cathode. *Chem* **4**, 2108–2123 (2018).
21. Liu, H. *et al.* A disordered rock salt anode for fast-charging lithium-ion batteries. *Nature* **585**, 63–67 (2020).
22. Lu, Y.-C. *et al.* In situ ambient pressure x-ray photoelectron spectroscopy studies of lithium-oxygen redox reactions. *Sci Rep.* **2**, 715 (2012).
23. Zhou, Y. *et al.* Real-time mass spectrometric characterization of the solid–electrolyte interphase of a lithium-ion battery. *Nat. Nanotechnol.* **15**, 224–230 (2020).
24. Urban, A., Lee, J. & Ceder, G. The configurational space of rocksalt-type oxides for high-capacity lithium battery electrodes. *Adv. Energy Mater.* **4**, 1400478 (2014).

25. van de Walle, A. & Ceder, G. Automating first-principles phase diagram calculations. *JPE* **23**, 348 (2002).
26. Brorsson, J., Zhang, Y., Palmqvist, A. E. C. & Erhart, P. order–disorder transition in inorganic vlathrates controls electrical transportproperties. *Chem. Mater.* **33**, 4500–4509 (2021).
27. van de Walle, A., Asta, M. & Ceder, G. The alloy theoretic automated toolkit: A user guide. *Calphad* **26**, 539–553 (2002).
28. Naoi, K., Ishimoto, S., Isobe, Y. & Aoyagi, S. High-rate nano-crystalline $\text{Li}_4\text{Ti}_5\text{O}_{12}$ attached on carbon nano-fibers for hybrid supercapacitors. *J. Power Sources* **195**, 6250–6254 (2010).
29. Kim, H.-S. *et al.* Oxygen vacancies enhance pseudocapacitive charge storage properties of MoO_{3-x} . *Nature Mater.* **16**, 454–460 (2017).
30. Fletcher, S., Black, V. J. & Kirkpatrick, I. A universal equivalent circuit for carbon-based supercapacitors. *J Solid State Electrochem* **18**, 1377–1387 (2014).
31. Kim, J., Nithya Jeghan, S. M. & Lee, G. Superior fast-charging capability of graphite anode via facile surface treatment for lithium-ion batteries. *Microporous and Mesoporous Mater.* **305**, 110325 (2020).
32. Zhang, N. *et al.* Facile preparation of nanocrystalline $\text{Li}_4\text{Ti}_5\text{O}_{12}$ and its high electrochemical performance as anode material for lithium-ion batteries. *Electrochem commun* **13**, 654–656 (2011).
33. Liu, J. *et al.* $\text{Li}_2\text{TiSiO}_5$ and expanded graphite nanocomposite anode material with improved rate performance for lithium-ion batteries. *Electrochim. Acta* **260**, 695–702 (2018).
34. Come, J. *et al.* A non-aqueous asymmetric cell with a Ti_2C -based two-dimensional negative electrode. *J. Electrochem. Soc.* **159**, A1368 (2012).
35. Lou, S. *et al.* High-rate capability of three-dimensionally ordered macroporous $\text{T-Nb}_2\text{O}_5$ through Li^+ intercalation pseudocapacitance. *J. Power Sources* **361**, 80–86 (2017).
36. Armstrong, A. R., Armstrong, G., Canales, J., García, R. & Bruce, P. G. Lithium-ion intercalation into $\text{TiO}_2\text{-B}$ nanowires. *Adv. Mater.* **17**, 862–865 (2005).
37. Yoo, H. D. *et al.* Intercalation pseudocapacitance of exfoliated molybdenum disulfide for ultrafast energy storage. *ChemNanoMat* **2**, 688–691 (2016).
38. Hao, Z. *et al.* Functional separators regulating ion transport enabled by metal-organic frameworks for dendrite-free lithium metal anodes. *Adv. Funct. Mater.* **31**, 2102938 (2021).

39. Wang, R. *et al.* Engineering layer structure of MoS₂-graphene composites with robust and fast lithium storage for high-performance Li-ion capacitors. *Energy Stor. Mater.* **9**, 195–205 (2017).
40. Shao, M. *et al.* Pushing the energy output and cycling lifespan of potassium-ion capacitor to high level through metal-organic framework derived porous carbon microsheets anode. *Adv. Funct. Mater.* **30**, 2006561 (2020).
41. Shao, Y. *et al.* Design and mechanisms of asymmetric supercapacitors. *Chem. Rev.* **118**, 9233–9280 (2018).
42. Dsoke, S., Fuchs, B., Gucciardi, E. & Wohlfahrt-Mehrens, M. The importance of the electrode mass ratio in a Li-ion capacitor based on activated carbon and Li₄Ti₅O₁₂. *J. Power Sources* **282**, 385–393 (2015).
43. Hemmati, S. *et al.* 3D N-doped hybrid architectures assembled from 0D T-Nb₂O₅ embedded in carbon microtubes toward high-rate Li-ion capacitors. *Nano Energy* **56**, 118–126 (2019).
44. Kim, H.-K. *et al.* TiO₂-reduced graphene oxide nanocomposites by microwave-assisted forced hydrolysis as excellent insertion anode for Li-ion battery and capacitor. *J. Power Sources* **327**, 171–177 (2016).
45. Luo, J. *et al.* Pillared structure design of MXene with ultralarge interlayer spacing for high-performance lithium-ion capacitors. *ACS Nano* **11**, 2459–2469 (2017).
46. Sivakkumar, S. R. & Pandolfo, A. G. Evaluation of lithium-ion capacitors assembled with pre-lithiated graphite anode and activated carbon cathode. *Electrochim. Acta* **65**, 280–287 (2012).
47. Li, Y. *et al.* Leaf-Like V₂O₅ nanosheets fabricated by a facile green approach as high energy cathode material for lithium-ion batteries. *Adv. Energy Mater.* **3**, 1171–1175 (2013).
48. Kresse, G. & Furthmüller, J. Efficiency of ab-initio total energy calculations for metals and semiconductors using a plane-wave basis set. *Comput. Mater. Sci.* **6**, 15–50 (1996).
49. Perdew, J. P., Burke, K. & Ernzerhof, M. Generalized gradient approximation made simple. *Phys. Rev. Lett.* **77**, 3865–3868 (1996).
50. Dudarev, S. L., Botton, G. A., Savrasov, S. Y., Humphreys, C. J. & Sutton, A. P. Electron-energy-loss spectra and the structural stability of nickel oxide: An LSDA+U study. *Phys. Rev. B* **57**, 1505–1509 (1998).
51. Wang, L., Maxisch, T. & Ceder, G. Oxidation energies of transition metal oxides within the GGA U framework. *Phys. Rev. B* **73**, 195107 (2006).

52. Ganose, A. M., Jackson, A. J. & Scanlon, D. O. sumo: Command-line tools for plotting and analysis of periodic *ab initio* calculations. *J. open source softw.* **3**, 717 (2018).
53. Monkhorst, H. J. & Pack, J. D. Special points for Brillouin-zone integrations. *Phys. Rev. B* **13**, 5188–5192 (1976).
54. Sluiter, M. H. F. & Kawazoe, Y. Invariance of truncated cluster expansions for first-principles alloy thermodynamics. *Phys. Rev. B* **71**, 212201 (2005).
55. van de Walle, A. & Ceder, G. Automating first-principles phase diagram calculations. *JPE* **23**, 348 (2002).
56. Brorsson, J., Zhang, Y., Palmqvist, A. E. C. & Erhart, P. Order–disorder transition in inorganic clathrates controls electrical transport properties. *Chem. Mater.* **33**, 4500–4509 (2021).
57. van de Walle, A., Asta, M. & Ceder, G. The alloy theoretic automated toolkit: a user guide. *Calphad* **26**, 539–553 (2002).
58. Sluiter, M. H. F. & Kawazoe, Y. Invariance of truncated cluster expansions for first-principles alloy thermodynamics. *Phys. Rev. B* **71**, 212201 (2005).
59. Ji, H. *et al.* Hidden structural and chemical order controls lithium transport in cation-disordered oxides for rechargeable batteries. *Nat. Commun.* **10**, 592 (2019).
60. Huang, J. *et al.* Non-topotactic reactions enable high rate capability in Li-rich cathode materials. *Nat. Energy* **6**, 706–714 (2021).

Figures

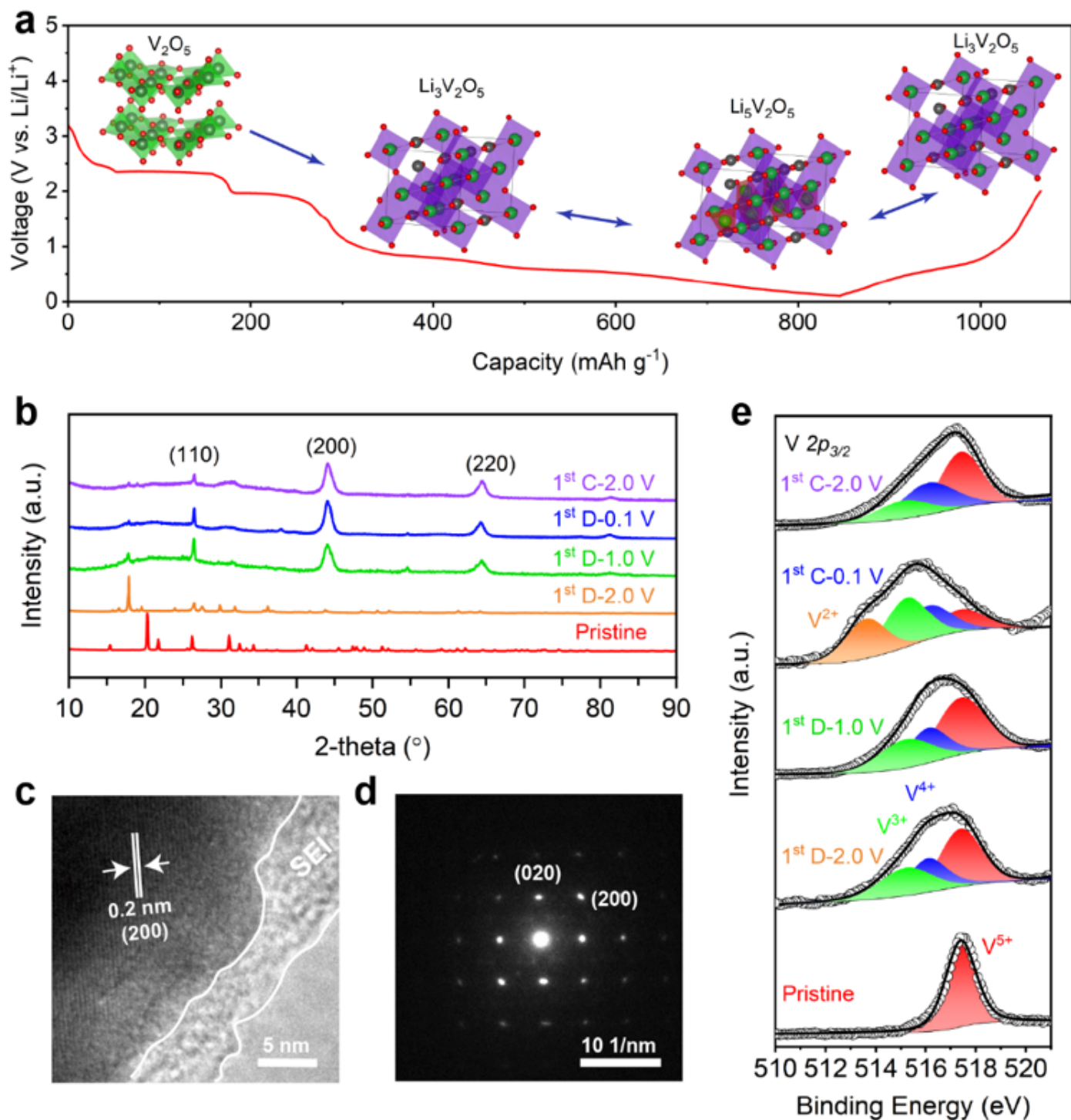


Figure 1

Structural properties of the as-prepared DRX-Li₃V₂O₅. **a** The typical voltage curve during the initial and followed lithiation/delithiation process. **b** Ex-situ XRD patterns of V₂O₅ during the initial cycle. **c** TEM image of DRX-Li₃V₂O₅ and **d** the corresponding electron diffraction (ED) image. **e** Ex-situ XPS spectra are measured at different lithiation and delithiation state during the initial cycle.

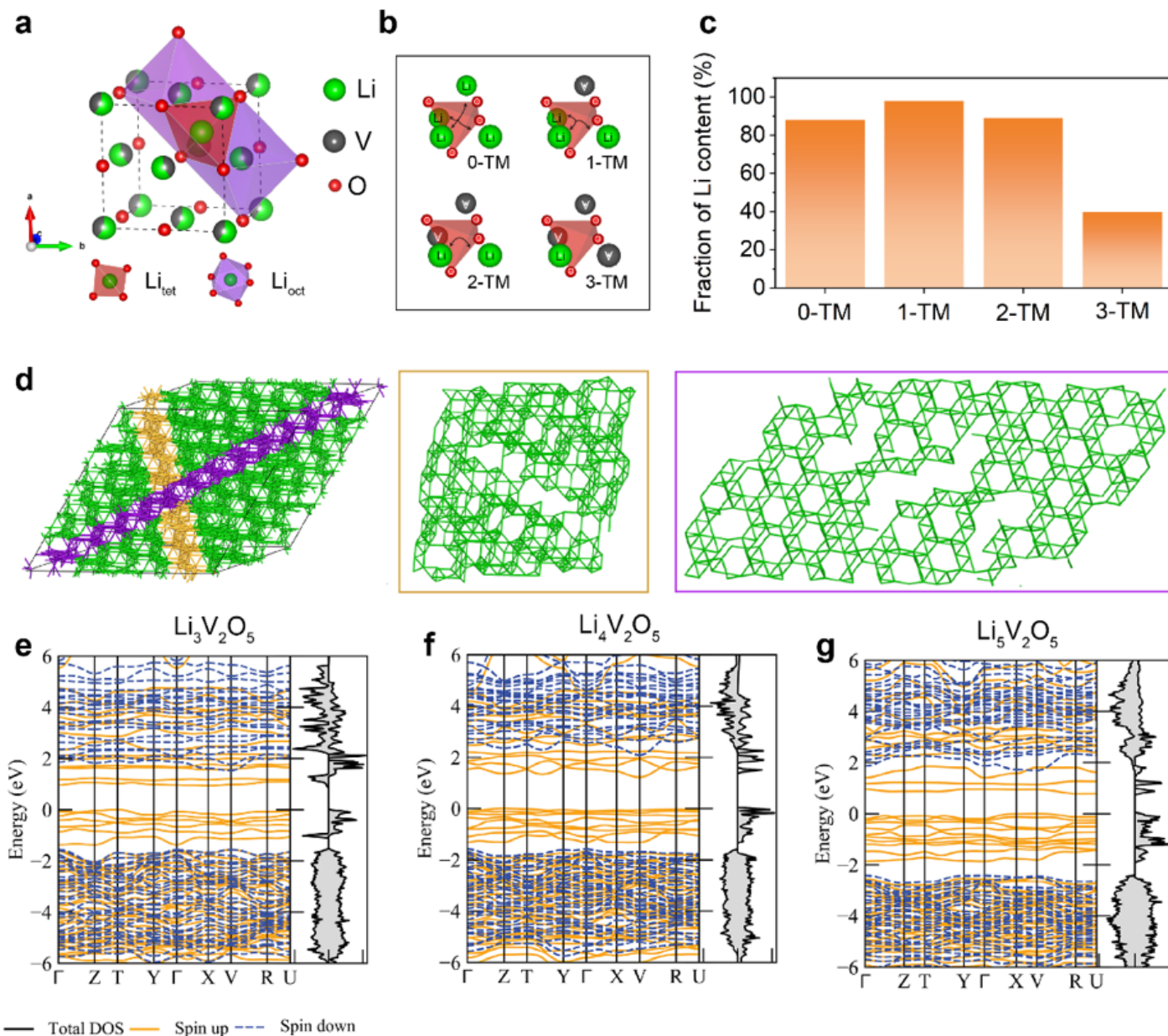


Figure 2

Results of the simulation. **a** Crystal structure of a DRX lithium metal oxide used to build cluster expansion. The black and green spheres can be occupied by Li or V atoms, and the red spheres represent O atoms. The black spheres represent V atom, the green spheres represent Li atom, and the red spheres represent O atom. **b** The crystal structures of 0-TM, 1-TM, 2-TM, and 3-TM tetrahedral clusters. **c** Li content in tetrahedral clusters (including 0-TM, 1-TM, 2-TM, and 3-TM) as the fraction of total Li sites. **d** Representative Monte Carlo simulated structures of $\text{Li}_x\text{V}_{5-x}\text{O}_5$ ($x=3$) at 300 K (only the atoms contained in 0-TM are shown), 0-TM connected Li atoms are bridged with green lines. Yellow and purple areas indicate the locations of the slices in the whole structure. The electronic properties (band structure and DOS) of **e** $\text{Li}_3\text{V}_2\text{O}_5$, **f** $\text{Li}_4\text{V}_2\text{O}_5$ and **g** $\text{Li}_5\text{V}_2\text{O}_5$.

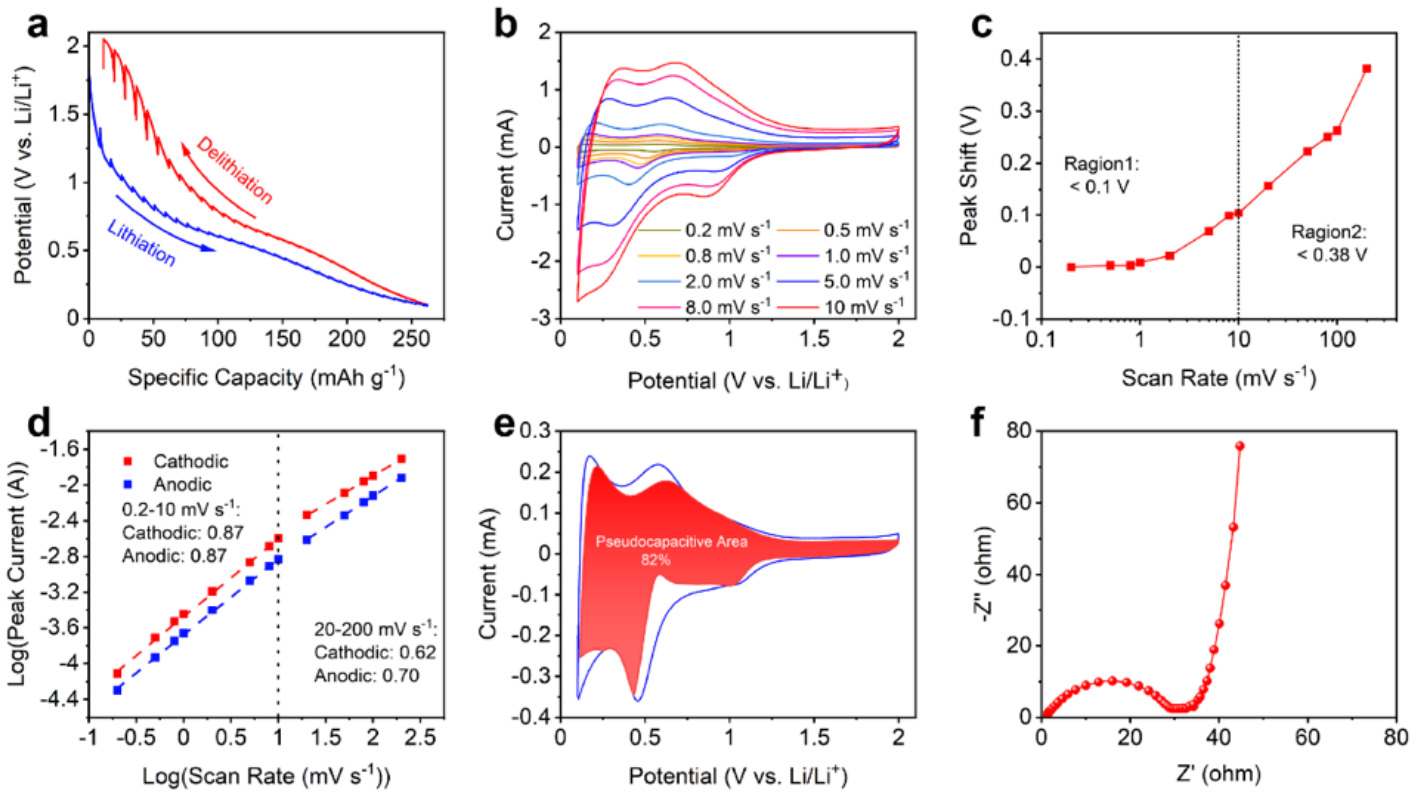


Figure 3

Kinetic properties of DRX-Li₃V₂O₅. **a** The potential response of DRX-Li₃V₂O₅ electrode during the galvanostatic intermittent titration technique (GITT) test at a current density of 0.1 A g⁻¹. **b** CV curves of DRX-Li₃V₂O₅ electrode. **c** The variation of anodic peak voltages with the different scan rates ranging from 0.2 to 100 mV s⁻¹. **d** *b*-values determination of the anodic and cathodic peak currents. **e** Voltametric response for DRX-Li₃V₂O₅ electrode at a sweep rate of 1 mV s⁻¹. The capacitive contribution to the total current is shown in the red region. **f** Nyquist plot of DRX-Li₃V₂O₅ achieved at 0.2 V (vs. Li/Li⁺).

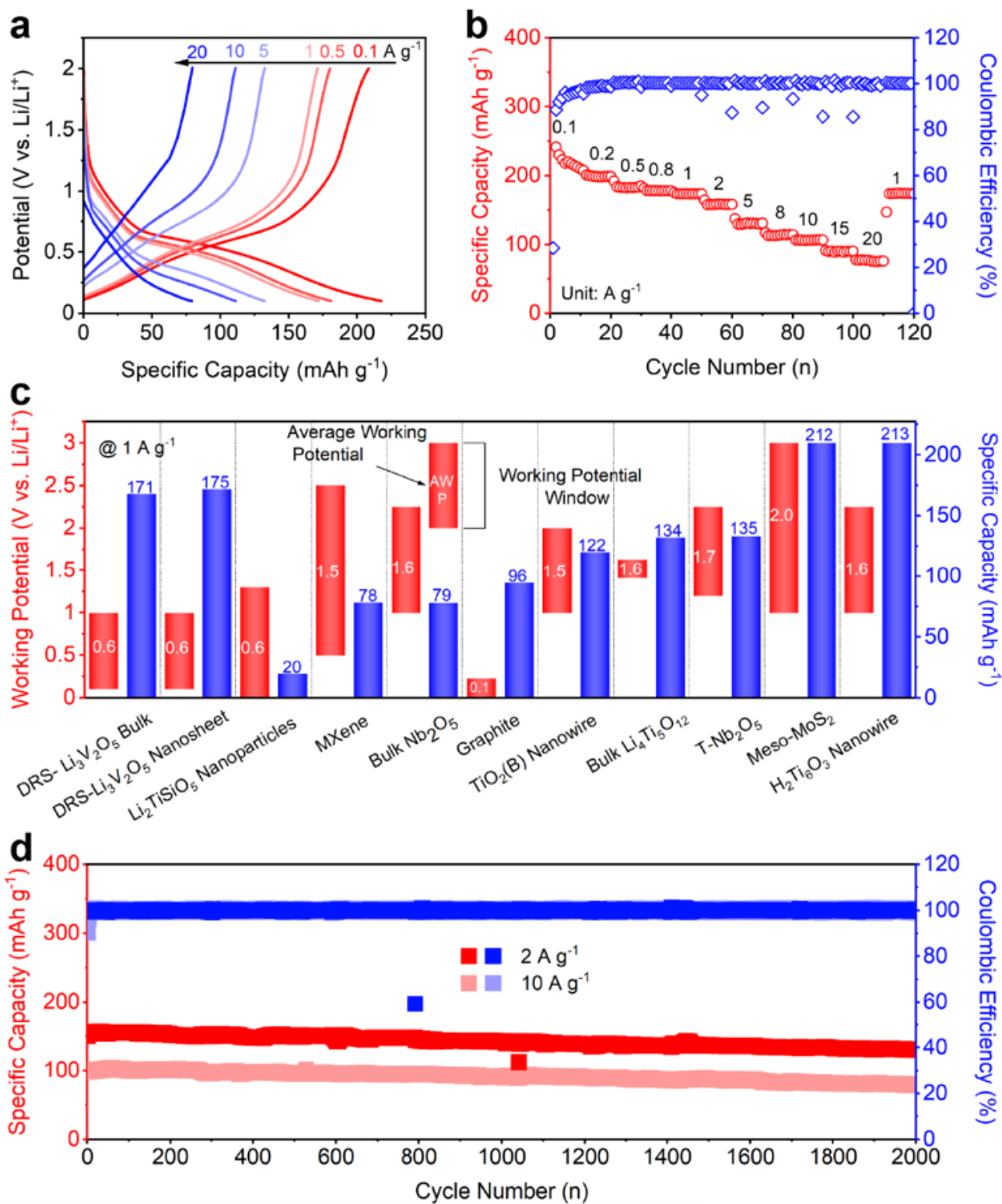


Figure 4

Electrochemical properties of DRX-Li₃V₂O₅. **a** Discharge–charge profiles at different current densities. **b** Rate capability from 0.1 to 20 A g⁻¹ for DRX-Li₃V₂O₅. **c** Specific capacity value and working potential range of DRX-Li₃V₂O₅ electrode and comparison with other commonly used anode materials. **d** Long-term cycle stability at 2 and 10 A g⁻¹.

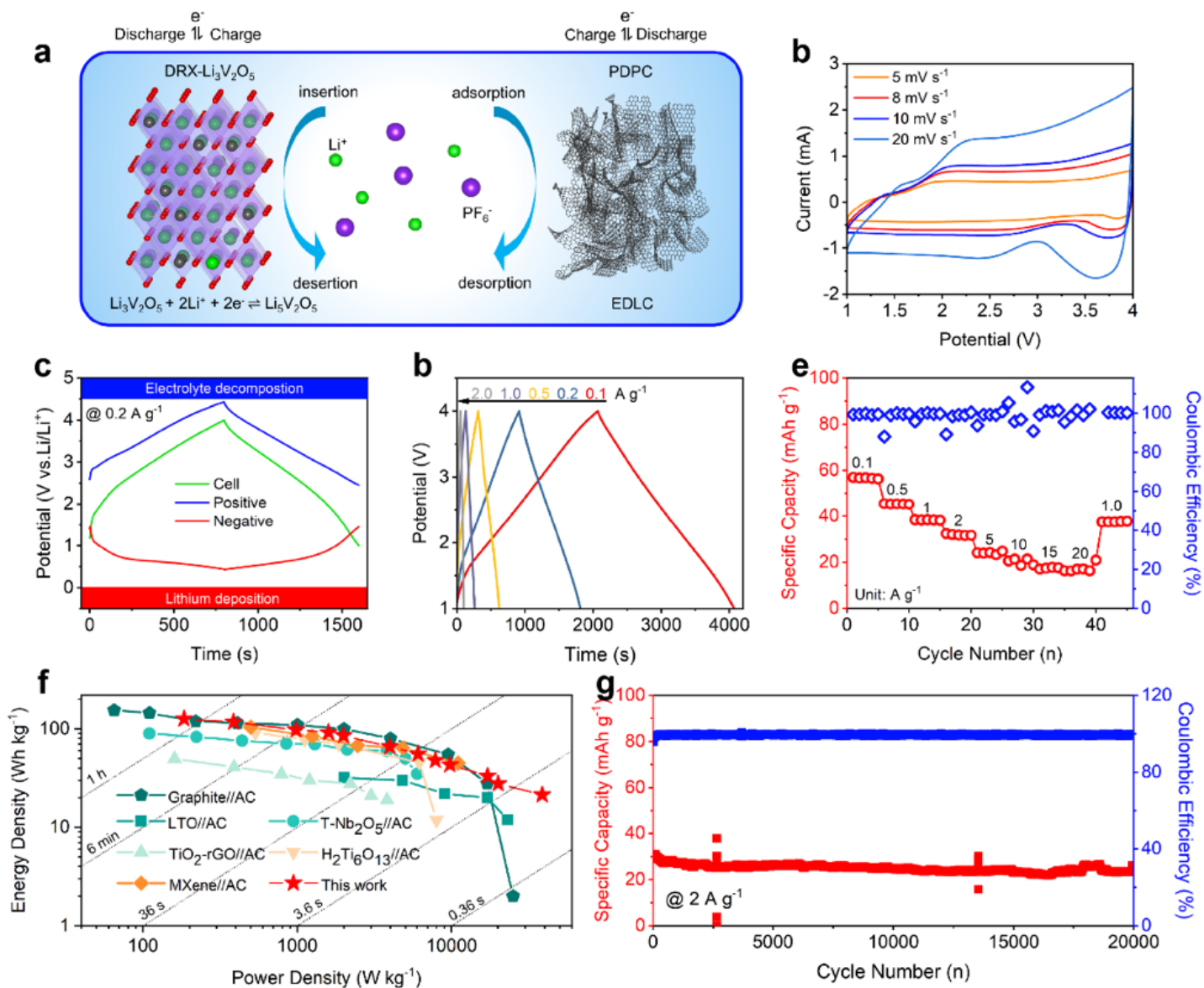


Figure 5

Capacity performance of DRX-Li₃V₂O₅//PDPC LIC in full-cell configuration. **a** Schematic image of the assembled full-cell device. **b** CV profile at the different sweep rates. **c** The potential swings for DRX-Li₃V₂O₅ (-), PDPC (+), and full cell recorded by three-electrode Swagelok cell at 0.2 A g⁻¹. **d** The galvanostatic charge/discharge profiles under different current densities. **e** Specific capacities under the different discharging current densities. **f** Ragone plots showing energy and power densities versus other reports. **g** Long-term cycling performance at 2 A g⁻¹.

Supplementary Files

This is a list of supplementary files associated with this preprint. Click to download.

- [SupportingInformation.docx](#)